Influence of nonmagnetic cation substitution on magnetic order temperature in Y-type hexaferrites: $Ba_{0.5}Sr_{1.5}Zn_2Fe_{12}O_{22}$ and $Ba_{0.5}Sr_{1.5}Zn_2Al_{0.08}Fe_{11.92}O_{22}$

Kiril Krezhov[1*], *Tatyana* Koutzarova[1], *Borislava* Georgieva[1], *Svetoslav* Kolev[1,2], *Daniela* Kovacheva[3], *Benedicte* Vertruyen[4], *Raphael* Closset[4], *Lan Maria* Tran[5], *Michał* Babij[5] and *Anatoliy* Senyshyn[6]

1Institute of Electronics, Bulgarian Academy of Sciences, 72 Tsarigradsko Chaussee, 1784 Sofia, Bulgaria

2Neofit Rilski South-Western University, 66 Ivan Mihailov Str.,2700 Blagoevgrad, Bulgaria

3Institute of General and Inorganic Chemistry, Bulgarian Academy of Sciences, Acad. Georgi Bonchev str., 1113 Sofia, Bulgaria

4Greenmat, Chemistry Department, University of Liege, 11 allée du 6 août, 4000 Liège, Belgium

5Institute of Low Temperature and Structure Research, Polish Academy of Sciences, Ul. Okólna 2, 50-422 Wroclaw, Poland

6TUZEFRM Forschungs-Neutronenquelle, Heinz Maier-Leibnitz (FRM II) 85748 Garching b. München, Lichtenbergstr. 1, Germany

Abstract. With a view to the proven multiferroic properties of the title representatives of the Y-type hexaferrites as single crystals we present here a comparative study of their microstructure and magnetic properties for powders. The polycrystalline materials of $Ba_{0.5}Sr_{1.5}Zn_2Fe_{12}O_{22}$ (S1) and its doped with aluminium derivative $Ba_{0.5}Sr_{1.5}Zn_2Al_{0.08}Fe_{11.92}O_{22}$ (S2) were synthesized by two different techniques: citric-acid sol-gel auto-combustion and sonochemical co-precipitation. Their atomic-level structure determination was checked by X-ray and neutron diffraction, electron diffraction and imaging methods, and their physical characterization was carried out by magnetometry. SEM images show that the microstructure strongly depends on the method of synthesis: non-uniform hexagonal grans are formed in case of auto-combustion whereas particles of nearly perfect hexagonal shape are observed in case of sonochemical co-precipitation. With lowering the temperature to 5 K several magnetic phase transitions were observed, more clearly pronounced in S2 powders. Neutron diffraction data in vicinity and above room temperature help in revealing the effect of magnetic dilution on the observed magnetic properties.

---

*Corresponding author: kiril.krezhov@gmail.com

1 Introduction

Hexaferrites are an important class of magnetic oxides with diverse applications, the most attractive of which have been in permanent magnets [1], data storage and energy conversion [2,3]. Particular performance of their properties was emphasized for devices operating at microwave frequencies to mitigate electromagnetic pollution, and to enrich the stealth technology [4]. Their rich crystal chemistry and a complex structural topology made them the subject of interest in solid state science since their discovery in the 1950s. The search for multiferroics, materials in which at least two of the ferroic order parameters, including ferroelectricity, ferromagnetism and ferroelasticity, coexist and interact has added momentum and extended the scope because of high potential for new applications [5,6]. For instance, if the coupling between the electric polarization P and magnetization M is sufficiently strong one might control the magnetic phase by applying an external electric field (E), as well as to influence the electric phase by applying an external magnetic field (H). This cross-coupling effect (magneto-electric effect) gives additional functionality to materials and opens up new possibilities in spintronics [6-9]. However, in most multiferroics, the sizeable magneto-electric (ME) effect usually occurs in the low temperature range and at applied external fields that are too high to be of practical use. Also, from the practical point of view of using multiferroics in multifunctional devices, it is important to control the electrical polarization or dielectric constant using weak magnetic fields or to manipulate the magnetization by an E field at temperatures near and above room temperature.

The discovery of multiferroic behaviour of particular single-phase representatives of nearly all main types of the hexaferrite family have substantially deepened the research efforts in the study of properties of single crystals with M-, Y -, Z- [10-17], and U -type structure [18]. The measured value of magnetic field driven electric polarization was not very large, amounting generally up to several tens of $\mu C/m^2$. Kitagawa et al. [19] presented the low-field ME effect in $Sr_3Co_2Fe_{24}O_{41}$ polycrystalline ceramics (representative of Z-type hexaferrites) sintered in oxygen atmosphere, where the electric polarization was $P_s \sim 1 \times 10^{-3}$ $\mu C/cm^2$ at 0.25 T. In the Y-type hexaferrite $Ba_2Mg_2Fe_{12}O_{22}$, Ishiwata et al. [15] demonstrated that a low magnetic field of 300 Oe is sufficient to reverse P indicating a well pronounced ME effect. With proven significantly large ME coupling in the near-ambient temperature range are the Y-type hexaferrites $Ba_{0.5}Sr_{1.5}Zn_2(Fe_{1-x}Al_x)_{12}O_{22}$ (x=0 and 0. 08). First, Kimura et al. [14] reported H-induced ferroelectric (FE) polarization in the undoped compound x=0 in a magnetic field of 0.1 T. Later, Chun et al. [20] measured in the magnetically diluted compound x=0.08 the largest ME coefficient in single-phase hexaferrites: α_H = 20,000 ps/m. It should be noted that a large ME coefficient is observed in $Ba_{0.4}Sr_{1.6}Mg_2Fe_{12}O_{22}$ single crystal with a value of 33,000 ps/m at 10 K [21], which is believed to be due

to a successful tuning of the spin cone symmetry in Y-type hexaferrites.

The atomic and magnetic order of the Y-type hexaferrite multiferroics has been well documented for single crystals. The results were elaborated by magnetic, diffraction, and Mössbauer studies. As commented in the recent review [22], due to the competition of exchange interactions and magnetic anisotropies several specific magnetic phases were determined to stabilize in particular temperature ranges, which can further be modified by applied magnetic field. Some of these phases exhibit room temperature spin-driven ferroelectricity [23] that according to the classification of Khomskii [24] corresponds to a type-II magnetoelectric coupling originated from complex magnetic orders.

Xu et al [25] investigated the substitution effects for polycrystalline $Ba_{0.5}Sr_{1.5}Zn_2(Fe_{1-x}Al_x)_{12}O_{22}$ with x=0, 0.04, 0.08 and 0.12 obtained by the conventional ceramic method, but their results were affected by the clear presence of Z and M-type phases in addition to the main Y- phase. To a large extent, these by-products of the synthesis with complex structure and magnetic behaviour accompany the very narrow temperature range for successful Y-phase formation, starting at 900ºC and ending at 1200ºC [2].

The subject of the present study are powder materials with x=0 and 0.08 prepared by soft chemistry routes. We summarize here the main results from our comparative studies of the structural and magnetic properties complemented with range-limited powder neutron diffraction measurements in the near and above room temperature range.

2 Experimental part

We prepared the $Ba_{0.5}Sr_{1.5}Zn_2Fe_{12}O_{22}$ (S1) and $Ba_{0.5}Sr_{1.5}Zn_2Al_{0.08}Fe_{11.92}O_{22}$ (S2) by citrate sol-gel auto-combustion method and sonochemical co-precipitation followed by thermal annealing. The resulting powder materials were characterized by X-ray diffraction (XRD) and neutron diffraction (ND) complemented by scanning electron microscopy (SEM) and magnetic measurements.

The metal nitrates ($Ba(NO_3)_2$ (99%), $Sr(NO_3)_2$ (99%), $Zn(NO_3)_2 \cdot 6H_2O$ (98%), $Al(NO_3)_{3x} \cdot 9H_2O$ (98%) and $Fe(NO_3)_{3x} \cdot 9H_2O$ (ACS, 98.0-101.0%), Alfa Aesar) were used as starting materials for the sol-gel auto-combustion. Deionised water was used as solvent for preparing solutions, and citric acid acted as combustion agent. The citric acid solution was slowly added to the mixed solution of nitrates as a chelator to form stable complexes with the metal cations. The solution was slowly evaporated to form a gel. This gel was dehydrated at 120°C to obtain the barium-strontium-zinc-(aluminium)-iron citrate precursor. During the dehydration process, the gel turned into a fluffy mass and was burnt in a self-propagating combustion manner. The auto-combusted powders were subsequently calcined for 7 hours at 1170°C in air.

Alternatively, stoichiometric amounts of the corresponding metal nitrates were dissolved in

deionized water and the co-precipitation process of metal cations was initiated by adding NaOH at pH = 12. High power ultrasound generated by a Sonics VCX 750 ultrasonic processor was applied for 15 minutes at a wave amplitude of 40% to assist the coprecipitation process. The obtained precursors were calcined at temperature of 1170°C in air for 7 hours.

In both routes of sample preparation, thermal annealing was completed by cooling the furnace to room temperature. To determine the morphology of the samples and the size and shape of the particles, SEM images were taken using an electron microscope system FEI XL30 FEG-ESEM.

The phase purity of the final materials as well as their crystal structures was analysed from room-temperature powder X-ray diffraction (XRD) data by Topas 4.2. The XRD patterns were collected in a Bruker D8 Advanced (filtered Cu radiation; 40 kV, 40 mA) diffractometer in Bragg-Brentano geometry equipped with a LynxEye PSD detector. Polycrystalline samples in batches of 3 g were used for the powder diffraction experiments on the SPODI diffractometer at the FRM II research reactor. The data were acquired at wavelengths of λ = 1.5482 Å and 2.537 Å down to d-values of 0.81 Å and 1.33 Å, respectively. The magnetic order evolution in the samples contained in thin-walled niobium cans was followed by successive data sets collected at 298 K, 300 K, 500 K, 900 K and 1000 K. The reduced data were treated by the Rietveld method [26] realized in the FullProf software package [27].

The M -H and M -T measurements without electric (E) field were carried out in a commercial Magnetic Property Measurement System (MPMS, Quantum Design). Isothermal magnetization curves were taken at selected temperatures. Zero-field-cooled (ZFC) and field-cooled (FC) magnetization curves vs. temperature (4.2 – 300 K) were measured at magnetic fields of 50 Oe, 100 Oe and 500 Oe. In the ZFC protocol, the sample was cooled from room temperature to 4.2 K in zero magnetic field and the magnetization was measured during warming from 4.2 - 300 K at a heating rate of 3 K/min in applied magnetic field. The FC curve was measured while warming after cooling the sample from 300 K to 4.2 K in applied magnetic field.

3 Results and discussion

The investigation of the crystal structure and morphology of samples, obtained via a sol-gel auto combustion method, was the subject of our recent work [28]. Also, some results on the magnetic properties of the compositions x=0 and x=0.08 have been reported previously [29, 30]. We found that even at the small studied level of aluminium doping, the long range atomic and magnetic order depend on the particular soft chemistry synthesis route as well as on the temperature and duration of the annealing. Here, only the most important magnetic and structural characteristics related and relevant to this work are presented.

The Ba$_{0.5}$Sr$_{1.5}$Zn$_2$Fe$_{12-x}$Al$_x$O$_{22}$ (x=0 and 0.08) compositions have a large structural unit cell (centric space group R-3m) with hexagonal lattice constants a = a′ ≈ 5.85 Å and c ≈ 43.46 Å, which is typical for the Y-type hexaferrite structure depicted in **Fig. 1(a)**. The unit cell contains 3 formula units (Z=3). The crystal structure is highly modular consisting of a superposition of hexagonal (T) and spinel (S) blocks along the c-axis direction. The unit cell is composed of a sequence of TST′ST″S″ blocks, with the primes indicating rotation by 120 degrees about c-axis **[2].** It has an easy axis of magnetization lying in a plane normal to the c-axis direction. The complete magnetic structure is shown to be greatly simplified by employing block-spin approximation; it is constructed by two magnetic sublattice blocks, one with a large net magnetization, L, and the other, S, with a small net magnetization, stacked alternatively along the [001] axis. These two magnetic blocks have opposite magnetizations, causing ferrimagnetism of the compounds above room temperature, and in their zero-field-cooled state host the non-polar alternating longitudinal conical (ALC) and proper-screw (PS) phases.
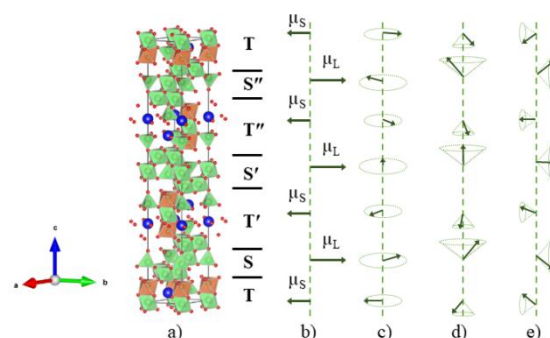

Fig. 1. (a) Schematic crystal structure of Y-type hexaferrite; (b) the collinear ferrimagnetic structure consists of alternate stacks of two spin blocks with μ$_L$ (larger magnetic moments) and μ$_S$ (smaller magnetic moments) along the c axis. (c) and (d) represent the non-polar spin order phases with propagation vector **k$_0$** parallel to c-axis: proper screw (PS) and alternate longitudinal conical (ALC) structure, respectively, exhibited at lower temperatures, (e) the transverse conical structure sensitive to external magnetic field.

The XRD diagrams of S1 and S2 powders showed the presence of the well crystalized Y-type hexaferrite structure as a main phase. The sonochemistry method yielded patterns of a hexaferrite structure with sharper and stronger peaks than the sol-gel auto-combustion.

Fig. 2 illustrates the X-ray diffractograms of undoped composition. The refined lattice parameters of the main phase in the R-3m space group with hexagonal settings were a=5.849(2)Å, c=43.555(3) Å and a=5.842(3)Å, c=43.681(3) Å for the auto-combustion and sonochemistry route, respectively. The few extra peaks labelled as a minor phase were identified as belonging to the spinel ZnFe$_2$O$_4$ amounting to less than 2.7 wt.% (standard card ICSD-04-006-1956). The detailed analysis by TOPAS using FWHM and integral breadths yielded a volume-

weighted mean crystallite size L = 200 ± 30 nm and a spinel lattice parameter of 8.4332(4) Å.
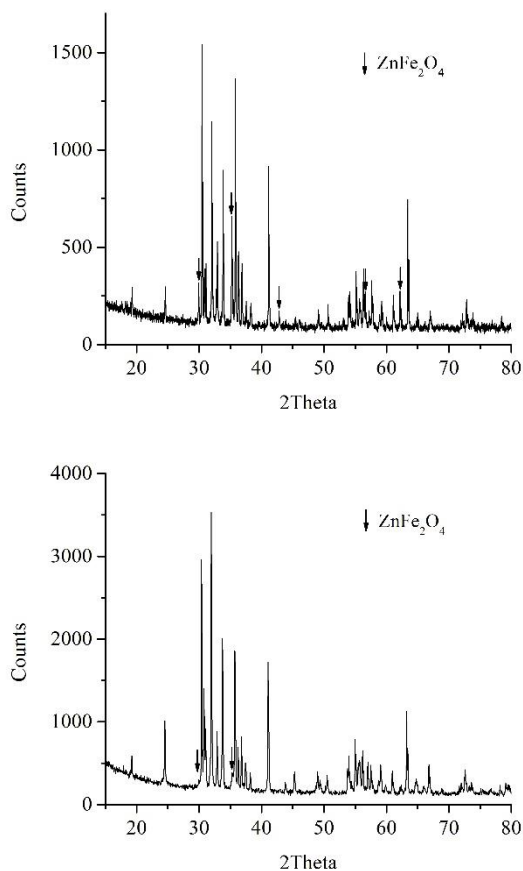

Fig. 2. XRD spectra of S1: (a) sol-gel auto-combustion, (b) sonochemistry [30].

In general, hexagonal grains were observed in the SEM images of both S1 and S2 samples. SEM images (Fig. 3a) of the S1 sample obtained by auto-combustion show particles of a very non-uniform shape and well-agglomerated to form clusters of different sizes and shapes. The average particle size varied between 200 nm and 1 μm with a mean 548 nm.
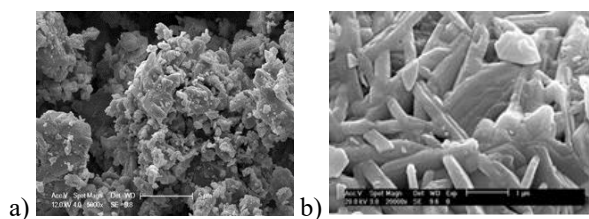
Fig. 3. SEM images of S1 obtained by auto-combustion (a) and by sonochemical co-precipitation (b) [29].

In contrast, the particles in the S1 sample obtained by sonochemical co-precipitation had the perfect hexagonal shape typical for hexaferrites (Fig. 3b), with a particle size of 996 nm and an average thickness of 168 nm. One observes that a three-dimensional grain growth process had taken place, together with co-growth of the particles resulting in plate-like grains which stack on each other.

As seen in Fig.4a, the Al-substitution led to a melting process at 1170 $^{\circ}$C for the S2 sample obtained by auto-combustion. Most of the particles are larger than 2 μm with different shape. Smaller particles of about 450 nm around the larger ones is also observed. On the other hand, the S2 material obtained by sonochemical co-precipitation (Fig.4b) consists of both particles of various size and shape, and of particles with a complete hexagonal shape. The hexagonal particles are in the range 1-2 μm long and are thin with a thickness of 50-70 nm. The plate-like hexagonal particles are well stuck together along the *c* axis to form an ensemble with a thickness well in excess of 100 nm.
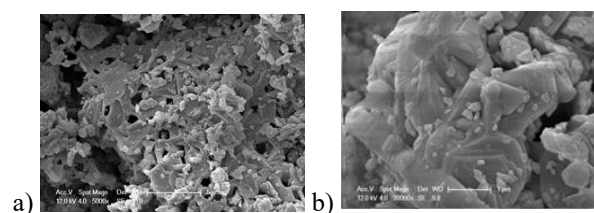

Fig. 4. SEM images of S2 obtained by auto-combustion (a) [29] and by sonochemical co-precipitation (b) [28].

More specifically, sol–gel auto-combustion and sonochemical synthesis yielded polydomain S1 and S2 particles, with an incomplete or rather plate-like elongated hexagonal shape, respectively; however, their thickness is sufficient to not feel the possible influence of surface defects (via a significant imbalance of the long-range spin ordering) on the magnetic phase transitions.

Figure 5 shows the magnetic hysteresis loops of undoped compound measured at 4.2 K and 300 K. For each preparation route, the saturation of magnetization is achieved above 30 kOe. The sonochemical material manifests a higher saturation magnetization M_s and coercive field H_c reflecting the dominant presence of particles with a superior hexagonal shape.

a)
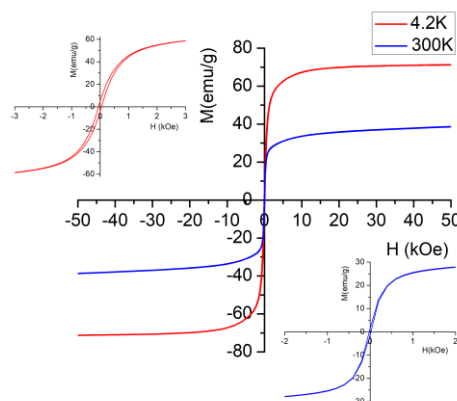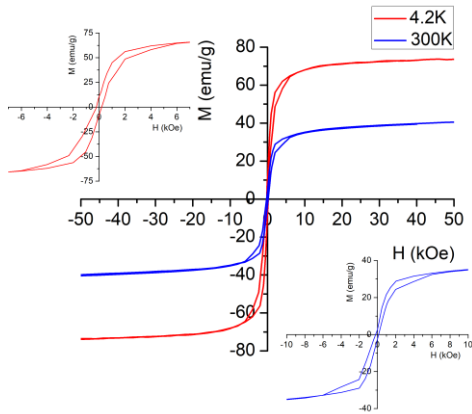
Fig. 5. Hysteresis loops of S1 powders obtained by (a) sol-gel auto-combustion and (b) sonochemistry.

Unlike typical ferromagnetic substances, Figure 6 shows a triple hysteresis loop that indicates the presence of two kinds of magnetic phases in S2 by sonochemical co-precipitation. We associate this type of hysteresis at 300K at low magnetic fields to the intermediate spin arrangement between the PS and the ferrimagnetic spin order presented schematically in Fig. 1.

It should be noted that, in contrast, a triple hysteresis loop was recorded by Xu et al [25] for their ceramic sample $Ba_{0.5}Sr_{1.5}Zn_2(Fe_{1-x}Al_x)_{12}O_{22}$ with x=0.08 in magnetic fields from 0 to 0.5 T but at 5 K.
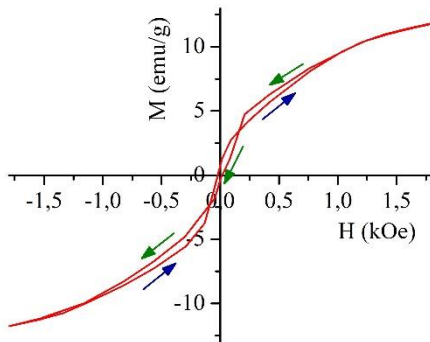

Fig. 6. Expanded view of the triple hysteresis curve at 300 K of S2 obtained by ultrasonically-assisted co-precipitation in the low magnetic field range disclosing the presence of two magnetic states [28].

Below the temperature of 326 K, the ferrimagnetic order in $Ba_{0.5}Sr_{1.5}Zn_2Fe_{12}O_{22}$ single crystals transforms into the helical spin order (see Fig. 1, c), in which the spin moments lie and rotate in the *ab*-plane [5, 9,13]. In a magnetic field applied perpendicular to the *c* axis, several magnetic transitions were found to take place in different temperature ranges, among which the so-called intermediate III phase shows a finite value of P.

Several anomalies of the magnetic behavior in the temperature range from 4.2 K to 300 K were observed for both S1 and S2 powders as presented in Figs 7-10 which can be understood in terms of the findings in single crystals.

Figure 7 shows the temperature variation of magnetization revealing the main regions of magnetic

phase transitions occurring in similar temperature ranges as described for single crystals by Kimura et al [5,14] and Chun et al [17, 20].
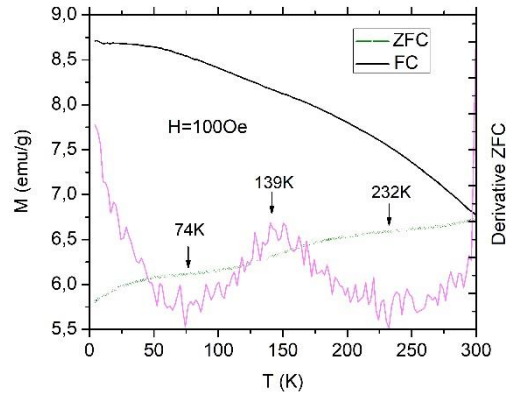

a)
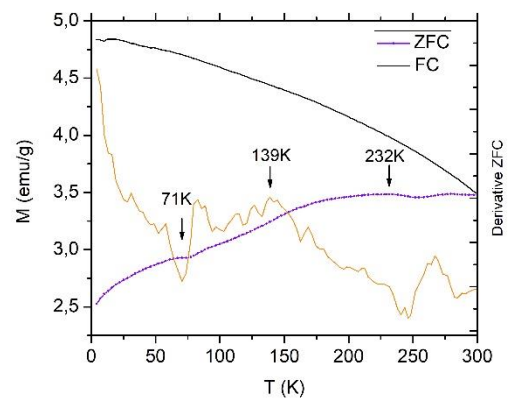
b)

Fig. 7. ZFC- and FC-magnetization vs temperature at 100 Oe for S1 obtained by (a) sol-gel auto-combustion and (b) sonochemistry [30]

Figure 8 illustrates the variation of the ac differential magnetization of S2 synthesized by sonochemical co-precipitation. By going down with temperature, the anomaly at about 285 K is to be associated with changes of magnetic arrangement from the collinear ferrimagnetic to the proper-screw spin phase while the behaviour between 85 K and 120 K is to be related with setting in the alternating longitudinal conical phase.
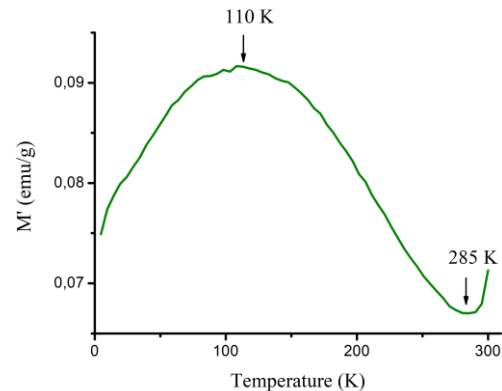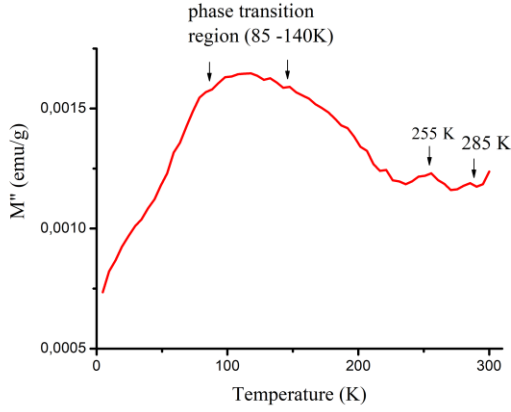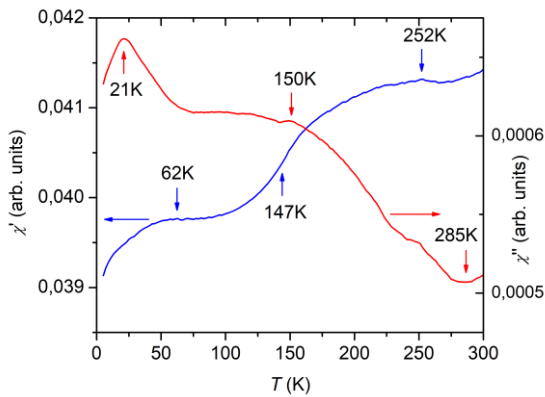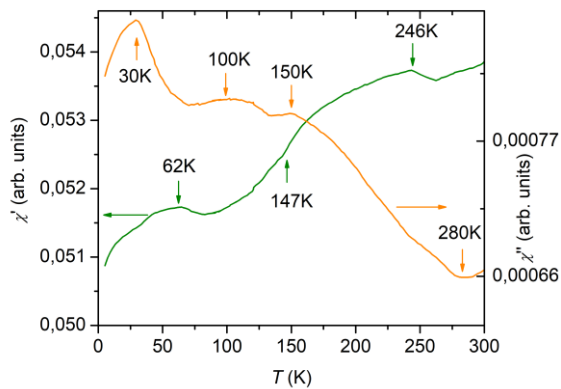
Fig. 8. Real part M' and imaginary part M" of ac differential magnetization of S2 obtained by sonochemistry vs temperature at H=10 Oe, f=1 kHz [28]

a)

b)

Fig. 9. The differential ac susceptibility of S1 obtained by (a) sol-gel auto-combustion and (b) sonochemistry in ac magnetic field of 10 Oe and frequency of 1 kHz. [30]
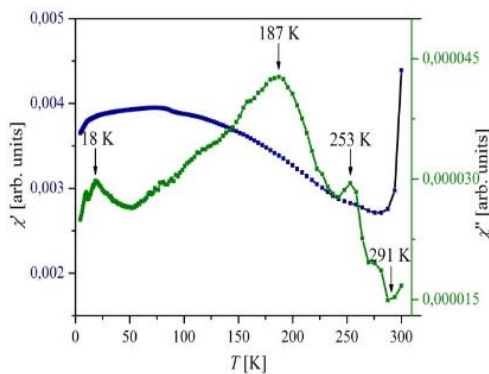

Fig. 10. The differential ac susceptibility of S2 obtained by sol-gel auto-combustion in ac magnetic field of 10 Oe and frequency of 1 kHz.

Expectedly, since the properties of the polycrystalline sample are an average of those of individual particles (taking into account the particles size distribution and their random or preferred orientation in the polycrystalline samples), the magnetic phase transitions are smoother compared to those of single crystals.

The results support the conclusion that the differences in the shape and size of the particles of the investigated soft chemistry products do not affect substantially the critical temperature of the various magnetic transitions observed in single crystals. But for the sonochemical samples, the transitions are much better pronounced due to the regular hexagonal shape of the constituent particles characteristic of hexaferrites, and the detection of metamagnetic transitions is facilitated.

The three-dimensional magnetic ordering in the Al substituted for Fe^{3+} Zn_2Y-type hexaferrite prepared by the two wet chemistry routes is clearly noticeable by the presence of additional peaks at 298 K, which rapidly lose intensity at higher temperatures as exemplified by Fig. 11.
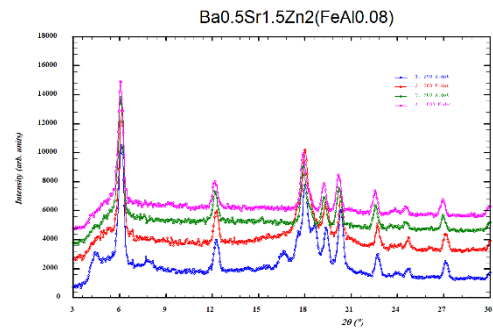

Fig. 11. Low angular part of neutron diffraction patterns of S2 collected on SPODI (MLZ) at selected temperatures. The presence of additional reflections at 298 K, which are purely magnetic in nature, is evident; they were attributed to the helicoidal arrangement formed by block-spins in the FE phase.

Due to the weak magnetic peak intensities, uncertainties in the propagation vector **k** at this stage introduce ambiguity in the associated spin ordering. Nevertheless, this finding is consistent with the low-field magnetization measurements for both S1 and S2 where the ZFC curve is observed to split from the FC curve above 300 K. For single crystal the transition from commensurate magnetic order to an incommensurate planar helix has been reported to occur at 310 K [12]. However, above 300 K we have ND measurements at temperatures of 500 K, 900 K, and 1000 K, where no satellite was observed but only Bragg peaks at wave vectors satisfying the condition - $h+k+l = 3n$, n integer. Therefore, from the present data we can confidently say that the helicoidal configuration disappears, but we cannot assert at what temperature in the range 320-290 K this magnetic transition takes

place, although the temperature range is seemingly extended to a higher temperature as compared with the results of Xu et al. [25,31] for their x=0.08 ceramic material and Chang et al. [32] for single crystals $Ba_{0.7}Sr_{1.3}Zn_2(Fe_{1-x}Al_x)_{12}O_{12}$ ($0 \leq x \leq 0.12$). Going up with temperature we observe the magnetic contribution to persist at 500 K indicating the expected ferrimagnetic order, $k_0=(0,0,0)$, and at 900 K and 1000 K there are diffraction intensities of nuclear Bragg peaks only.
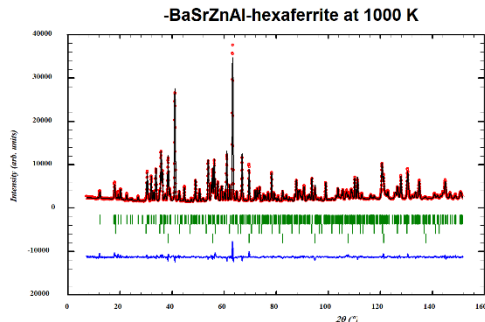

Fig. 12. Rietveld refined neutron powder diffraction pattern of S2 at 1000 K (λ = 1.5482 Å). Traces of zinc ferrite and Nb container were also considered. The series of tick marks correspond to the allowed Brag reflections.

Fig.12 illustrates the Rietveld refined neutron diffraction pattern of S2 in the paramagnetic region at 1000 K. No regions were excluded from the refinement. As variable parameters, the structural model takes into account the partial substitution of Fe occupying tetrahedral sites with Zn and Fe occupying octahedral sites with Al. The plate-like morphology of the particles observed in the SEM images is reflected strongly in the neutron diffraction lines.

4 Summary

Zn_2Y-type hexaferrite polycrystalline material of high crystallinity $Ba_{0.5}Sr_{1.5}Zn_2Fe_{12-x}Al_xO_{22}$ (x=0 and 0.08) was produced by two wet chemistry routes followed by thermal annealing. Sonochemistry yielded samples consisting of particles characterized predominantly by the hexagonal shape typical of hexaferrites. Accordingly, M_s and H_c were higher for those powders. The differential AC susceptibility shows specific peaks indicating magnetic phase transformations, and this feature is more pronounced for the powder produced by sonochemistry. Four kinds of hysteresis loops can be observed in $Ba_{0.5}Sr_{1.5}Zn_2Al_{0.08}Fe_{11.92}O_{22}$ revealing the occurrence of magnetization processes of different magnetic spin structures in given temperature ranges. The magnetic structures of both compositions studied are qualitatively similar and differ mainly in the non-collinear arrangement of iron spins especially those in octahedral sites of the Y-type hexaferrite structure. Neutron diffraction data present clear evidence for the destruction of the helical spin structure between 298 K and 300 K.

5 References

1. C. de Julián Fernández, C. Sangregorio, J. de la Figuera, B. Belec, D. Makovec, A. Quesada, J. Phys. D: Appl. Phys. **54**, 153001 (2021)

2. R.C. Pullar, Prog. Mater. Sci. **57**, 1191 (2012)

3. N.A. Spaldin, Proc. R. Soc. A **476**, 20190542 (2020)

4. P. Sahoo, L. Saini, A. Dixit, Oxford Open Materials Science **3**, itac012 (2023)

5. T. Kimura, Annu. Rev. Condens. Matter Phys. **3**, 93 (2012)

6. N.A. Spaldin, R. Ramesh, Nature Mater **18**, 203–2 (2019)

7. A. Hoffmann, S.D. Bader, Phys. Rev. Appl. **4**, 047001 (2015)

8. S. Fusil, V. Garcia, A. Barthélémy, M. Bibes, Ann. Rev. Mater. Res. **44**, 91 (2014)

9. F. Matsukura, Y. Tokura, H. Ohno, Nat. Nanotechnol. **10**, 209 (2015)

10. N. Momozava, Y. Yamaguchi, H. Takei, M. Mita, J. Phys. Soc. Jpn. **54**, 771 (1985)

11. N. Momozava, J. Phys. Soc. Jpn. **54**, 4007 (1986)

12. N. Momozava, Y. Yamaguchi, H. Takei, M. Mita, J. Phys. Soc. Jpn. **54**, 3895 (1985)

13. N. Momozawa, Y. Yamaguchi, J. Phys. Soc. Jpn **62**, 1292 (1993)

14. T. Kimura, G. Lawes, and A. P. Ramirez, Phys. Rev. Lett. **94**, 137201 (2005).

15. S. Ishiwata, Y. Taguchi, H. Murakawa, Y. Onose, and Y. Tokura, Science **319**, 1643 (2008)

16. M. Soda, T. Ishikura, H. Nakamura, Y. Wakabayashi, and T. Kimura, Phys. Rev. Lett. **106**, 087201 (2011)

17. S. H. Chun, Y. S. Chai, B.-G. Jeon, H. J. Kim, Y. S. Oh, I. Kim, H. Kim, B. J. Jeon, S. Y. Haam, J.-Y. Park et al., Phys. Rev. Lett. **108**, 177201 (2012)

18. K. Okumura, T. Ishikura, M. Soda, T. Asaka, H. Nakamura, Y. Wakabayashi, and T. Kimura, Appl. Phys. Lett. **98**, 212504 (2011)

19. Y. Kitagawa, Y. Hiraoka, T. Honda, T. Ishikura, H. Nakamura, and T. Kimura, Nat. Mater. 9, 797 (2010).

20. S. Chun, Y. Chai, Y. Oh, D. Jaiswal-Nagar, S. Haam, I. Kim, B. Lee, D. Nam, K-T Ko, J-H Park, J-H Chung, K. Kim, Phys. Rev. Lett. **104**, 037204 (2010)

21. K. Zhai, Y. Wu, S. Shen, W. Tian, H. Cao, Y. Chai, B. C. Chakoumakos, D. Shang, L. Yan, F. Wang, Y. Sun, Nat Commun. **12**, 519 (2017)

22. T. Koutzarova, S. Kolev, K. Krezhov, Ch. Ghelev, B. Vertruyen, L. M. Tran, A. Zaleski, *Preparation and phase transitions in Y-type magneto-electric hexaferrites*, Chapter 3, in book: *Advances in Materials Science Research*, Editor: Maryann C. Wythers, Publisher: Nova Science Publishers, Inc., **41**, 105 (2020)

23. V. Kocsis, T. Nakajima, M. Matsuda, A. Kikkawa, Y. Kaneko, J. Takashima, K. Kakurai, T. Arima, Y. Tokunaga, Y. Tokura, Y. Taguchi, Phys. Rev. B **101**, 075136 (2020)

24. D. Khomskii, Physics **2**, 20 (2009)

25. W. Xu, J. Yang, W. Bai, Y. Zhang, K. Tang, Chun-gang Duan, X. Tang, J. Chu, J. Appl. Phys. **117**, 17D909 (2015)

26. H. Rietveld, J. Appl. Crystallogr. **2**, 65 (1969)

27. J. Rodríguez-Carvajal, Physica B **192**, 55 (1993)

28. B. Georgieva, T. Koutzarova, S. Kolev, Ch. Ghelev, B. Vertruyen, R. Closset, R. Cloots, A. Zaleski, Bulg. Chem. Commun., **48 (G)**, 147 (2016)

29. B. Georgieva, S. Kolev, Ch. Ghelev, D. Kovacheva, B. Vertruyen, R. Closset, T. Koutzarova. *A Comparative study of the morphology of Y-type hexaferrite powders obtained by sol-gel auto-combustion and ultrasonic co-precipitation*. In Advanced Nanotechnologies for Detection and Defence against CBRN Agents, Petkov, P., Tsiulyanu, D., Popov, C., Kulisch, W., Ed.; NATO Science for Peace and Security Series B: Physics and Biophysics, Dordrecht, Springer, 2018; pp 31–36.

30. B. Georgieva, S. Kolev, K. Krezhov, Ch. Ghelev, D. Kovacheva, B. Vertruyen, R. Closset, L- M. Tran, M. Babij, A. J. Zaleski, T. Koutzarova, J. Magn. Magn. Mater. **477**, 131 (2019).

31. W. Xu, J. Yang, Y. Shen, W. Bei, Y. Zhang, J. Liu, K. Tang, Z. Wang, Ch.-g. Duan, X. Tang, J. Chu, AIP Advances 4, 067122 (2014.

32. H. Chang, H. B. Lee, Y.-S. Song, J.-H. Chung, S.A. Kim, I.H. Oh, J. Reehus, J. Schefer – Phys. Rev. B85, 064402 (2012)